Advanced Composites and Hybrid Materials (2021) 4:716–724
https://doi.org/10.1007/s42114-021-00301-5

ORIGINAL RESEARCH

Three-dimensional porous flower-like S-doped Fe_2O_3 for superior lithium storage

Zhaoqian Yan[1] · Zhihao Sun[1] · Anran Li[1] · Hongshou Liu[1] · Zihao Guo[1] · Lei Qian[1]

Received: 11 May 2021 / Revised: 30 June 2021 / Accepted: 1 July 2021 / Published online: 10 July 2021

Abstract
Traditional Fe-based oxide with poor intrinsic conductivity, severe volume expansion, and structure destruction exhibits the poor cyclic performance for anode materials of lithium ion batteries (LIBs). Heteroatomic doping Fe-based oxide with nanoarchitectures is deemed to settle the above problems effectively. Herein, with sulfur (S) doping, three-dimensional porous flower-like Fe_2O_3 (denoted as S- Fe_2O_3) prepared via ordinary solvothermal reaction and calcining process was ingeniously designed as anode materials for LIBs. The S doping changed the morphology, improved the electrical conductivity, and provided more active sites for lithium storage. The flower-like S-Fe_2O_3 made up of plentiful carbon encapsulated nanoparticles not only relieved the volume expansion but also provided the connected conductive network. The as-prepared flower-like S-Fe_2O_3 electrode delivered a high discharge/charge capacity (1570.8 mAh g^{-1} at 0.1 A g^{-1} after 100 cycles) and the excellent long-cycle performance (521.3 mAh g^{-1} at 2.0 A g^{-1} after 1000 cycles). S doping and nanoarchitectures engineering in this work provide rational preparation strategies for composites containing transition metal oxides toward energy storage system.

Keywords S doping · Fe_2O_3 · Flower-like morphology · Lithium ion batteries

1 Introduction

Lithium ion batteries (LIBs), the new secondary energy storage equipment, are applied in portable electronic equipment and large-scale electrical vehicle markets due to high energy density, environment-friendly, and low self-discharge [1–10]. However, the commercial graphite anode materials, with low specific capacity (372 mAh g^{-1}) and inferior security, could not satisfy the large demand for energy storage [11–13]. The task for exploring a high-energy density anode material to replace the traditional graphite is extremely challenging. In recent years, traditional Fe-based oxides with low cost, abundant raw materials, and non-toxic materials have been prospect and industrialization of anode materials [14–16]. Nevertheless, the poor intrinsic electrical conductivity and volume expansion immensely restrict the lithium storage performance of traditional Fe-based oxides.

Doping and nanoarchitectures engineering are promising methods in order to settle above unsatisfied problems [17–27]. The strategies of constructing nanoarchitectures and compositing with carbon materials can effectively guarantee the structural stability, shorten the diffusion distance of lithium ions, relieve volume expansion, and increase the conductivity [28–32]. Wu et al. reported the γ-Fe_2O_3 nanoparticles stabilized by holey reduce graphene oxide via using in situ etching route, which delivered a high reversible capacity of 1141 mAh g^{-1} at 0.5 A g^{-1} after 230 cycles [33]. Ju and co-workers reported composites of reduced graphene oxide and MoS_2 nanosheets modified by Fe_2O_3 nanoparticles, which delivered the capacity of 906 mAh g^{-1} at 0.2 A g^{-1} after 100 cycles [34]. Although the researchers have paid tremendous efforts, it cannot solve the problem fundamentally.

It is worth noting that doping engineering (cations and anions) has been used to regulate the morphology, enhance the electrical conductivity, and provided more active sites to improve the performance of LIBs [14, 35, 36]. Surface doping of cationic atoms can enhance the synergistic effect of metals and increase more active sites [36]. For example, Pan et al. prepared Cr-doped Fe_2O_3/reduced graphene oxide nanocomposites with high capacity of 1062 mAh g^{-1}

✉ Lei Qian
qleric@sdu.edu.cn

[1] Key Laboratory for Liquid-Solid Structural Evolution and Processing of Materials (Ministry of Education), Shandong University, 17923 Jingshi Road, Jinan 250061, China

at 0.1 g^{-1} over 180 cycles [14]. Ni and Co co-doped yolk-shell–type Fe_2O_3@TiO_2 hollow microspheres were synthesized by Qi et al., delivering the capacity of 562 mAh g^{-1} at 0.2 A g^{-1} after 200 cycles [37]. Anion atom doping can alter the distribution of charge within a crystal for electrode materials, improve the conductivity, and provide more Li adsorption sites [14, 35]. Due to the radius of sulfur (S) atoms higher than that of oxygen atoms, more space in traditional Fe-based oxide after S doping is conducive to better transfer of lithium ions and maintains the structure stability. The literature on S-doped Fe_2O_3 for LIBs has been rarely reported. For instance, Yang et al. constructed self-standing S-doped Fe_2O_3 for rechargeable NiCo-Fe batteries with high energy storage capacity [38].

Herein, with S doping, the three-dimensional porous flower-like Fe_2O_3 (denoted as S-Fe_2O_3) composites were prepared via oversimplified solvothermal method and calcining process for LIBs. This specific structure offered plentiful benefits: first, S doping modulated the inner electronic structure of Fe_2O_3, improved the intrinsic conductivity, provided more active sites, and facilitated the diffusion rate of Li ions. Second, the carbon shell–coated nanoparticles were anchored on micron flowers to form the original morphology. Benefit by the distinctive morphology, ultra-small nanoparticles decreased the diffusion distances; the interwoven carbon shell increased the electrical conductivity, impeded the agglomeration of particles, and relieved the volume expansion. As we expected, the flower-like S-Fe_2O_3 electrode delivered the excellent electrochemical performances.

2 Experimental

2.1 Chemical and reagents

Ferric chloride hexahydrate ($FeCl_3{\cdot}6H_2O$, AR), ethanol absolute (C_2H_6O, AR), and ethylene glycol (EG, $C_2H_6O_2$, AR) were purchased by Shanghai Sinopsin Group Chemical Reagent Co. LTD. Hexamethylenetetramine ($C_6H_{12}N_4$, ACS, 99%) was acquired from Shanghai Aladdin Industrial Company. Thiourea (H_2NCSNH_2, 99%) was bought from Tianjin Guangfu Science and Technology Development Co. LTD.

2.2 Preparation of flower-like S-Fe_2O_3

In the typical synthesis process, 0.27 g $FeCl_3{\cdot}6H_2O$ and 1 g $C_6H_{12}N_4$ were dissolved in 30-ml EG with stirring for 1 h to form the yellow clarification solution. Then, the mixed solution was transferred into 50-ml Teflon-lined stainless autoclave at 160 ºC for 8 h. The dark yellow precipitate was gathered with washing three times with anhydrous ethanol and deionized water after cooling to room temperature. Next, the as-prepared precipitate was dried at 60 ºC overnight (denoted as flower-Fe). The flower-Fe samples were heated up to 500 ºC for 2 h with the heating rate of 3 ºC/min to obtain the flower-like Fe_2O_3.

One hundred twenty milligrams thiourea was dissolved in 35 ml ethanol absolute with stirring for 30 min to get the transparent solution. Subsequently, 40 mg flower-like Fe_2O_3 was added into the above solution with ultrasound for 30 min. Later, the solution was loaded into the 50-ml Teflon-lined stainless autoclave at 180 ºC for 4 h. The sample was collected after cooling to room temperature via washing several times with ethanol absolute. Finally, the flower-like S-Fe_2O_3 was received by vacuum drying at 60 ºC for 8 h.

2.3 Characterization and apparatus

The phase analysis and composition of flower-like Fe_2O_3 and S-Fe_2O_3 were measure by X-ray diffraction (XRD, Miniflex 600, Japan, $\lambda = 1.5406$ Å). Field emission scanning electron microscope (FESEM, Hitachi SU-70, Tokyo, Japan) and transmission electron microscope (TEM, JEOL JEM-2100 F, Japan) were employed to characterize the morphology and structure of flower-like Fe_2O_3 and S-Fe_2O_3. X-ray photoelectron spectroscopy (XPS) was conducted with Thermo ESCALAB 250XI (USA). The specific surface area and pore structure of flower-like Fe_2O_3 and S-Fe_2O_3 materials were performed by N_2 adsorption/desorption isotherms with Micromeritics Instrument Corp ASAP2460.

2.4 Electrochemical measurements

Electrochemical performances of flower-like Fe_2O_3 and S-Fe_2O_3 samples were gained by assembling the 2032-type coin cells in glove box replenished with Ar gas. The cathode of half-cell was loaded with 70% active materials (flower-like Fe_2O_3 or S-Fe_2O_3), 20% super-P, and 10% polyvinylidene fluoride. The weight of active materials was 1.1 ± 0.2 mg. The lithium foils were picked as reference anode. The mixture of 1 M $LiPF_6$ in ethylene carbonate (EC) and diethyl carbonate (DEC) (1:1 in mass ratio) was used as electrolyte. The charge/discharge curves, rate, and cycle performances of flower-like Fe_2O_3 and S-Fe_2O_3 were measured by LAND CT2001A (China). The cyclic voltammetry (CV) and electrochemical impedance spectroscopy (EIS) curves of Fe_2O_3 and S-Fe_2O_3 hybrids were tested by CHI660D (China).

3 Results and discussion

3.1 Structural and morphological characterization

Figure 1 shows the synthesis process of the obtained flower-like S-Fe_2O_3 composite. First, the flower-Fe was prepared

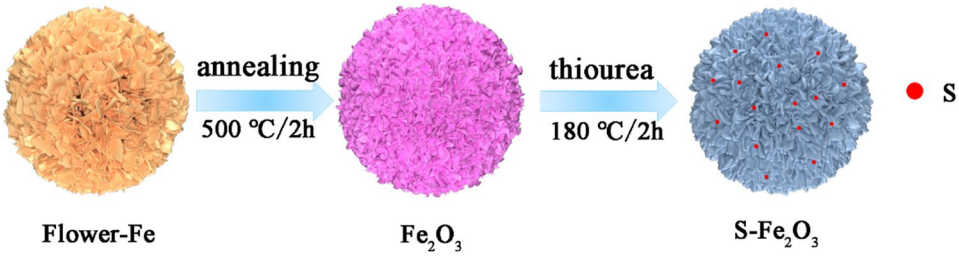

Fig. 1 Synthesis process of the flower-like S-Fe_2O_3 composites

via sample solvothermal reaction. Then, the flower-Fe sample was transformed into Fe_2O_3 by annealing process. Finally, the Fe_2O_3 product was doped by S atoms by hydrothermal reaction with thiourea.

The phase composition of as-prepared samples was characterized by XRD. Figure 2a monitors the XRD patterns of flower-like Fe_2O_3 and S-Fe_2O_3 hybrids. As you can see, all the sharp diffraction peaks located at 30.3, 35.7, 43.3, 53.8, 57.4, and 63.0 could be indexed to the lattice planes of (2 0 6), (1 1 9), (0 0 12), (2 2 12), (1 1 15), and (4 0 12), matching with the standard card (PDF no. 25–1402) of tetragonal γ-Fe_2O_3. N_2 adsorption–desorption isotherms were acquired to analyze the specific surface area and porosity of S-Fe_2O_3 hybrids. In Fig. 2b, N_2 adsorption–desorption isotherms were ascribed to the type IV hysteresis loop, revealing the mesoporous properties of S-Fe_2O_3 hybrids. The specific surface area of flower-like S-Fe_2O_3 was about 51.98 $m^2\ g^{-1}$. The pore-size distribution curves of flower-like S-Fe_2O_3 exhibited the pore size range of 1.57 to 25 nm and average pore diameter of 16.7 nm based on the Barrett-Joyner-Halenda (BJH) way (Fig. 2c). The large specific surface area and a mass of pore channels provided the more contacted area between the electrode and electrolyte. The valence states of elements on the sample surface were performed by XPS. Fig. S1a shows the survey spectrum of flower-like S-Fe_2O_3, indicating the existence of C, N, O, S, and Fe elements. The C 1s spectrum of flower-like S-Fe_2O_3 in Fig. S1b was fitted with four peaks at 284.6, 285.5, 286.4, and 288.7 eV corresponding to C = C, C–N, C–O, and O–C = O bonds [39, 40]. As shown in Fig. S1c, the N 1s spectrum of flower-like S-Fe_2O_3 exhibited that the peaks at 398.6, 399.9, and 401.2 eV were ascribed to the pyridinic-*N*, pyrrolic-*N*, and graphitic-*N* [41, 42]. In high-resolution Fe 2p spectra (Fig. 2d), the peaks situated at 710.8, 712.8, and 724.6 were

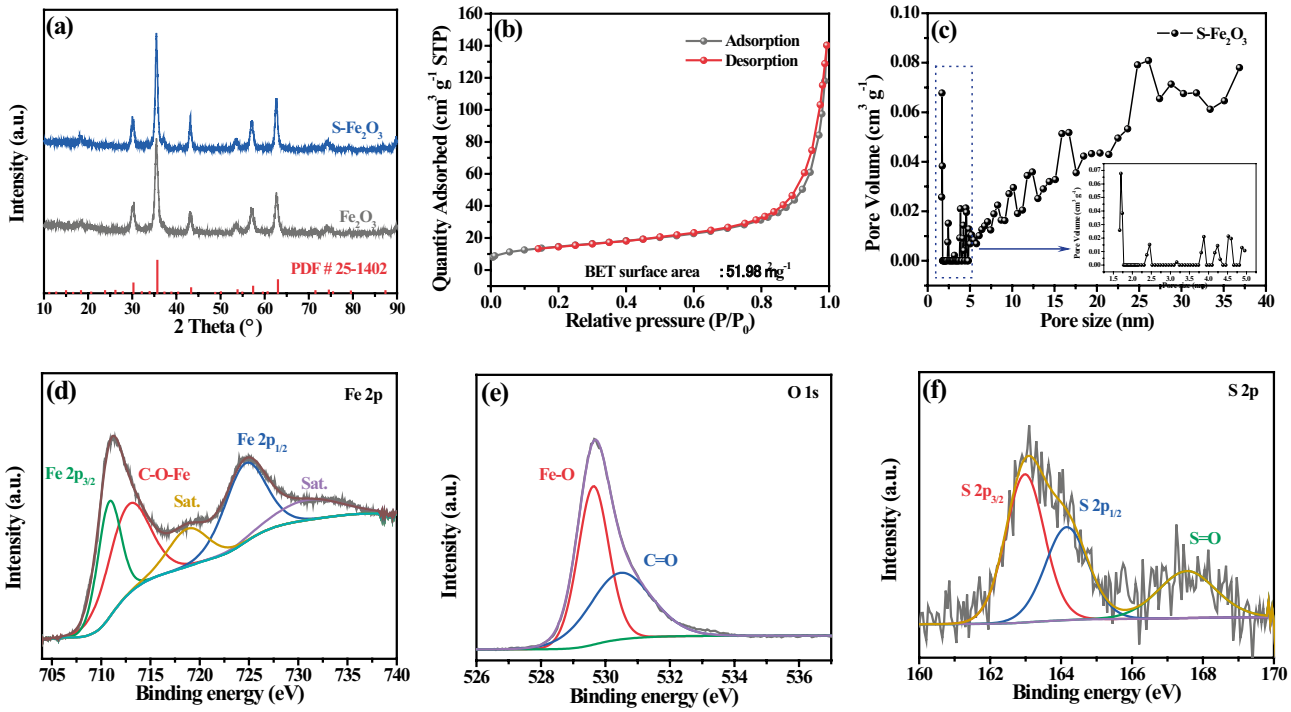

Fig. 2 XRD patterns of Fe_2O_3 and S-Fe_2O_3 (**a**); N_2 adsorption/desorption isotherms of S-Fe_2O_3 (**b**); the corresponding BJH pore size distribution of S-Fe_2O_3 (**c**); the high-resolution XPS spectra of S-Fe_2O_3: Fe 2p (**d**), O 1 s (**e**), and S 2p (**f**)

attributed to the main valence state (Fe $2p_{3/2}$, C–O–Fe, and Fe $2p_{3/2}$) [33, 43, 44]. The two satellites peaks were positioned at 718.8 and 730.5 eV. The O 1s spectrum of flower-like S-Fe_2O_3 displayed the peaks at 529.6 and 530.5 eV related to the Fe–O and C = O bonds (Fig. 2e) [34, 45, 46]. The S 2p spectrum of flower-like S-Fe_2O_3 demonstrated three typical peaks at 162.9, 164.2, and 167.5 eV (Fig. 2f), which were affiliated to the S $2p_{3/2}$, S $2p_{1/2}$ states and S = O bond, respectively [36, 38]. The XPS results proved that S atoms were successfully doped into Fe_2O_3.

The morphology and internal structure of as-synthesized samples were carried out by FESEM and TEM. As shown in Fig. S2a, the acquired flower-Fe was highly similar uniform morphology. The size of flower-Fe was about 2 µm, loaded with abundant nanosheets with the thickness of 30–40 nm (Fig. 3a). After annealing, the Fe_2O_3 samples still maintained the morphology of flower, and the nanosheets were wrinkled (Figs. 3b and S2b). Treated with thiourea, the obtained S-Fe_2O_3 samples could maintain a faint flower shape, and the thickness of the nanosheets became thicker (Figs. 3c, d and S2c), proving that the morphology of Fe_2O_3 was controlled by S doping. In Fig. 3e, the low-magnification TEM images of S-Fe_2O_3 sample confirmed the flower-like morphology with porous structure. And the flower-like S-Fe_2O_3 sample contained many homogeneous nanoparticles with the diameter of 15–20 nm (Fig. 3f). The high-resolution transmission electron microscopy (HRTEM) image of S-Fe_2O_3 is shown in Fig. 3g. The interplanar spacings of 0.25, 0.29, and 0.48 nm were associated to the lattice planes of (119), (206), and (113), corresponding to XRD patterns (Fig. 2a). Subsequently, the lattice distortion may be considered as the effect of S doping. Moreover, it was observed that the nanoparticles were uniformly coated by carbon shell. The selected area electron diffraction (SAED) image of flower-like S-Fe_2O_3 is shown in Fig. 3h. The diffraction rings of S-Fe_2O_3 were index to the lattice planes of (6 2 6), (4 0 12), (1 1 15), (1 1 9), (2 0 6), and (1 1 6) consistent with the XRD results and HRTEM images.

3.2 Electrochemical characterization

The lithium storage properties of flower-like Fe_2O_3 and S-Fe_2O_3 electrodes were evaluated with the coin-type half-cell. Figure 4a exhibits the first three CV curves of flower-like S-Fe_2O_3 anode at 0.2 mV s^{-1}. In the first cathode scanning process, the peaks at 1.41 and 0.88 V were associated with intercalation of Li^+ into the Fe_2O_3 to form $Li_xFe_2O_3$ and the transformation of Fe^{3+} to Fe^{2+}, respectively [5, 33]. And the peak at 0.68 V was ascribed to the formation of the solid electrolyte interface (SEI) films and the reduction of Fe^{2+} to Fe^0 [13, 15]. During the anodic scanning process, the peaks located at 1.63 and 1.8 V were attributed to the oxidation of Fe^0 to Fe^{2+} and further conversion of Fe^{2+} to Fe^{3+} [13, 45]. In the second cathode scanning process, the peaks were shifted to 0.79 and 0.96 V, corresponding to the transformation of Fe^{3+} to Fe^{2+} and Fe^{2+} to Fe^0. A well-coincident last two CV curves indicated a stable lithiation/delithiation process. The galvanostatic charge/discharge profiles of flower-like S-Fe_2O_3 for 1st, 3rd, 5th, 20th, 50th, and 100th cycle at the current density of 0.1 A g^{-1} are shown in Fig. 4b. The S-Fe_2O_3 electrode delivered the discharge/charge capacity of 1298.5/938.1 mAh g^{-1} for the first cycle with Coulombic efficiency of 72.3% higher than that of Fe_2O_3 electrode (68.5%). And the capacity loss

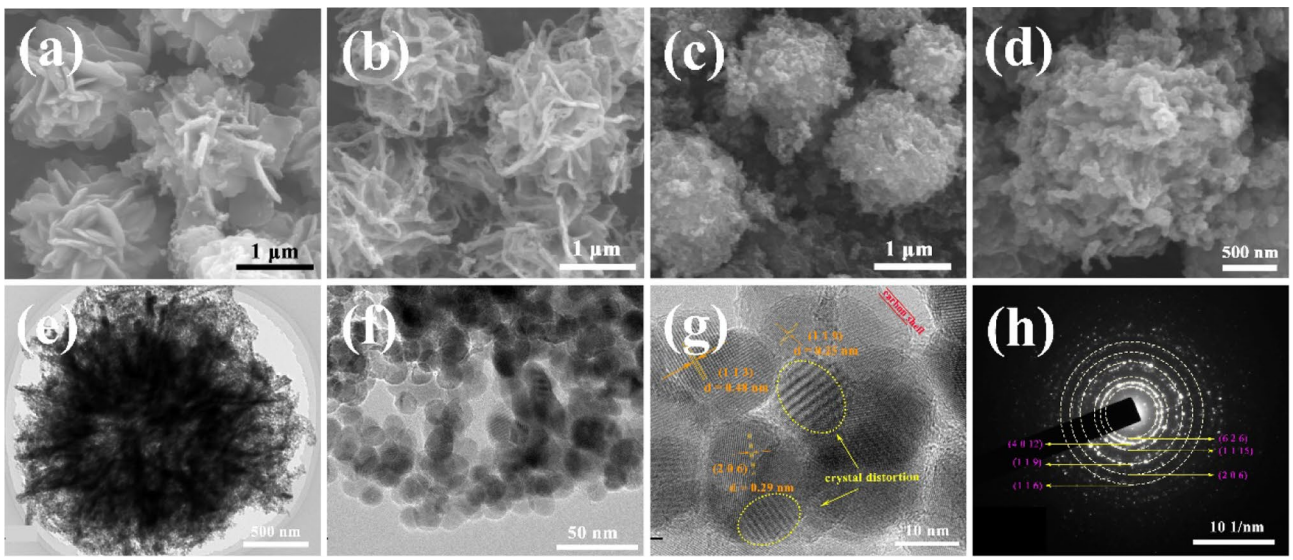

Fig. 3 FESEM images of flower-Fe (**a**), Fe_2O_3 (**b**) and S-Fe_2O_3 (**c**, **d**); TEM images of S-Fe_2O_3 (**e**, **f**); HRTEM images of S-Fe_2O_3 (**g**); SAED pattern of S-Fe_2O_3 (**h**)

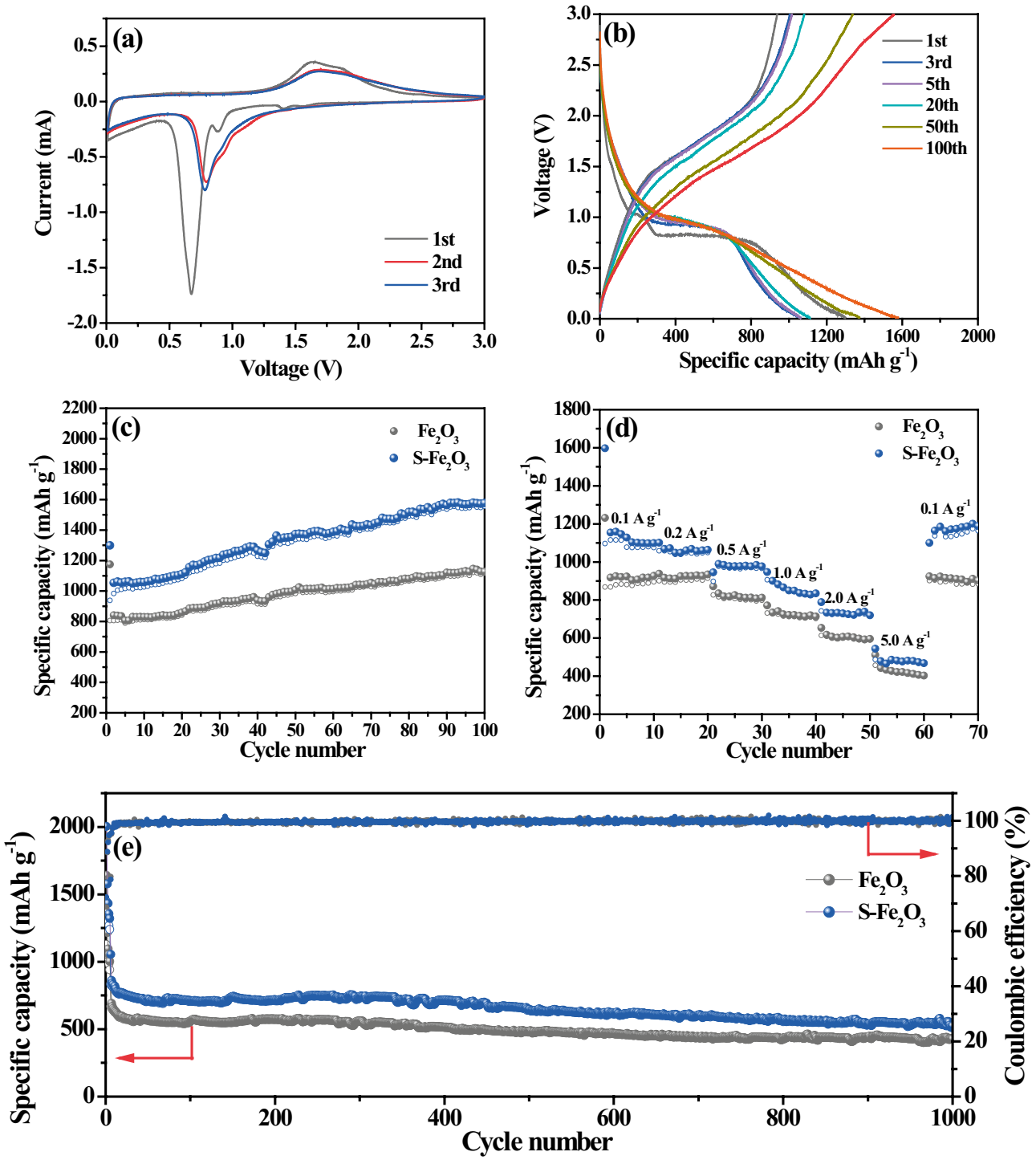

Fig. 4 CV curves for the first three cycles of S-Fe_2O_3 at 0.2 mV s^{-1} (**a**); galvanostatic charge/discharge profiles of S-Fe_2O_3 at the 1st, 3rd, 5th, 20th, 50th, and 100th at 0.1 A g^{-1} (**b**); cycle performance of Fe_2O_3 and S-Fe_2O_3 at 0.1 A g^{-1} (**c**); rate performances of Fe_2O_3 and S-Fe_2O_3 (**d**); long-cyclic performance of Fe_2O_3 and S-Fe_2O_3 at 2.0 A g^{-1} (**e**)

was attributed to the formation of solid electrolyte interphase (SEI) films [43, 46]. In addition, the voltage platforms were also corresponding to the peaks of CV curves (Fig. 4a). The cycle performances of Fe_2O_3 and S-Fe_2O_3 electrodes at 0.1 A g^{-1} after 100 cycles are shown in Fig. 4c, and the specific capacity of S-Fe_2O_3 electrode was obviously better than that of Fe_2O_3 electrode. In addition, the S-Fe_2O_3 electrode maintains the capacities of 1570.8 mAh g^{-1} after 100 cycles, demonstrating the remarkable lithium storage properties. The reason for capacity increase

of S-Fe_2O_3 and Fe_2O_3 electrodes possibly was attributed to intercalation/de-intercalation process in high-voltage, conversion reaction in low voltage and electrode activation [47–50]. Figure 4d displays the rate performances of Fe_2O_3 and S-Fe_2O_3 electrodes at various current densities. It was found that the S-Fe_2O_3 electrode delivered the higher capacities of 1099 (10th), 1063.7 (20th), 977.1 (30th), 734.6 (40th), 619.8 (50th), and 468.4 mAh g^{-1} at the current density of 0.1, 0.2, 0.5, 1.0, 2.0, and 5.0 A g^{-1}. The capacity still could recover to initial value when the current dropped down to 0.1 A g^{-1}, confirming the excellent rate performance. Figure 4e displays the long-term cycling performance of flower-like Fe_2O_3 and S-Fe_2O_3 electrode at 2.0 A g^{-1} after 1000 cycles. The S-Fe_2O_3 electrode delivered the higher capacity of 521.3 mAh g^{-1} than that of 424.0 mAh g^{-1} (Fe_2O_3), revealing good cyclic stability.

Figure 5a shows the electrochemical impedance spectroscopy (EIS) and the fitting curves of Fe_2O_3 and S-Fe_2O_3 hybrids. Obviously, according to circuit diagram (R(QR)(Q(RW))), the fitted results are shown in Table S1. And the R_{ct} value of S-Fe_2O_3 was lower than that of Fe_2O_3, exhibiting the higher charge transfer capacity owing to the existence of S doping. To further pursue the sources of high-rate performance, the CV curves of S-Fe_2O_3 and Fe_2O_3 electrodes at various scanning rates from 0.2 to 1.0 mV s^{-1} are identified in Figs. 5b and S3a. The high capacities of S-Fe_2O_3 and Fe_2O_3 electrodes were related to the pseudo-capacitance and diffusion behaviors according to the Randles–Sevcik Eq. (1) [11, 17]:

$$i = av^b \tag{1}$$

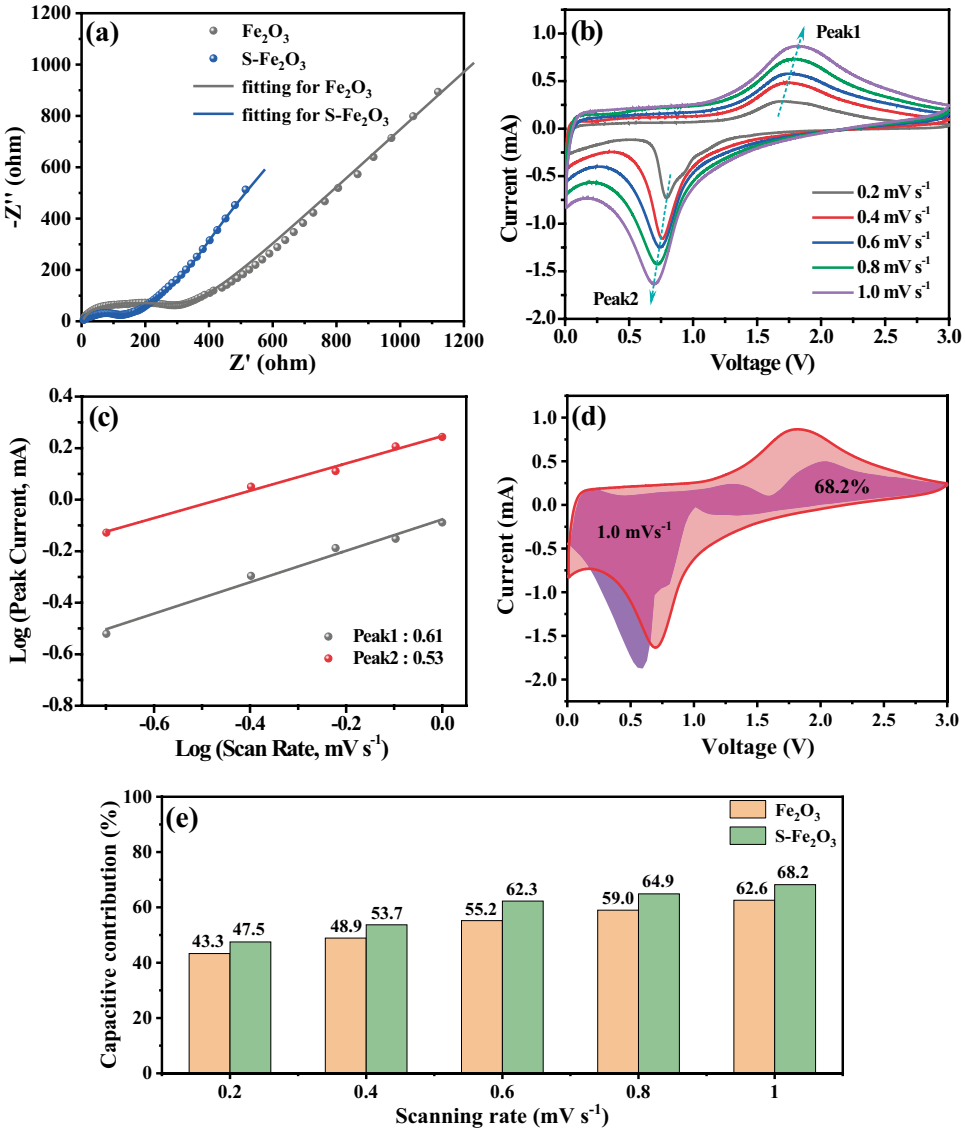

Fig. 5 Electrochemical impedance spectra of Fe_2O_3 and S-Fe_2O_3 (**a**); CV curves of S-Fe_2O_3 electrode at different scan rates of 0.2–1.0 mV s^{-1} (**b**); fitting curves of the b-values of S-Fe_2O_3 (**c**); capacitive contributions under purple shaded areas of S-Fe_2O_3 electrode at the scanning rate of 1.0 mV s^{-1} (**d**); the contribution ratio of capacitive capacities for Fe_2O_3 and S-Fe_2O_3 electrode at different scan rates (**e**)

Herein, the b = 0.5 represents the diffusion process, and the b = 1.0 is on behalf of pseudo-capacitance behavior. However, the value of b between 0.5 and 1.0 indicates that the electrochemical reactions are controlled by both pseudo-capacitance and diffusion behaviors. According to CV curves of S-Fe_2O_3 and Fe_2O_3 electrodes during different sweeping speed (Figs. 5b and S3a), the b values of peak1 and peak2 were obtained and are shown in Figs. 5c and S3b. All the b values were between 0.5 and 1.0, which declared the influence of two kinds of behaviors. The specific pseudo-capacitance and diffusion contributions of S-Fe_2O_3 and Fe_2O_3 electrodes were also calculated by Eq. (2) [12, 18]:

$$i = k_1 v + k_2 v^{1/2} \quad (2)$$

Herein, k_1v is interrelated to the pseudo-capacitance contribution, and $k_2v^{1/2}$ is attached to the diffusion process. In Figs. 5d and S3c, the higher pseudo-capacitance contribution of 68.2% (S-Fe_2O_3) than that of 65.8% (Fe_2O_3) at the scanning rate of 1.0 mV s^{-1} was obtained. In Fig. 5e, the pseudo-capacitance contribution of S-Fe_2O_3 electrode increased from 47.5 to 68.2% with the scanning rate increasing from 0.2 to 1.0 mV s^{-1}, which was higher than that of Fe_2O_3 electrode (43.3 to 62.6%), ascribed to more active sites induced by S doping. Fig. S4 shows the FESEM images of S-Fe_2O_3 electrode at 0.1 A g^{-1} after 100 cycles. Clearly, the S-Fe_2O_3 electrode maintained the original shape, demonstrating a stable structure.

4 Conclusions

In this paper, the three-dimensional porous flower-like S-doped Fe_2O_3 composites were fabricated successfully by solvothermal method and high-temperature annealing process. The composition and microstructures of S-Fe_2O_3 composites were conducted by XRD, TEM, XPS, and FESEM. Doping of S atoms changed the electron structure of Fe_2O_3 and provided the more active sites for lithium storage. A micron flower composed of plentiful carbon shell–coated nanoparticles enhanced electrical conductivity, relieved the volume change, and provided a variety of diffusion channels of Li ions. As expected, the flower-like S-Fe_2O_3 electrode delivered the high specific capacity (1570.8 mAh g^{-1} after 100 cycles at 0.1 A g^{-1}) and outstanding long-cycle performance (521.3 mAh g^{-1} at 2.0 A g^{-1} after 1000 cycles). The synergistic control of morphology and doping is a reasonable way to fabricate high-performance TMO composites.

Supplementary information The online version contains supplementary material available at https://doi.org/10.1007/s42114-021-00301-5.

Funding This work was supported by the National Natural Science Foundation of China of China (No. 51672162).

Declarations

Competing interests The authors declare no competing interests.

References

1. Jin H, Xin S, Chuang C, Li W, Wang H, Zhu J, Xie H, Zhang T, Wan Y, Qi Z, Yan W, Lu Y, Chan T, Wu X, Goodenough JB, Ji H, Duan X (2020) Black phosphorus composites with engineered interfaces for high-rate high-capacity lithium storage. Science 370:192–197
2. Xu H, Zhao L, Liu X, Huang Q, Wang Y, Hou C, Hou Y, Wang J, Dang F, Zhang J (2020) Metal-organic- framework derived core-shell N-doped carbon nanocages embedded with cobalt nanoparticles as high-performance anode materials for lithium-ion batteries. Adv Funct Mater 30:2006188
3. Liu H, Zhu Z, Yan Q, Yu S, He X, Chen Y, Zhang R, Ma L, Liu T, Li M, Lin R, Chen Y, Li Y, Xing X, Choi Y, Gao L, S-y CH, An K, Feng J, Kostecki R, Amine K, Wu T, Lu J, Xin HL, Ong SP, Liu P (2020) A disordered rock salt anode for fast-charging lithium-ion batteries. Nature 585:63–67
4. Liu X, Zhao L, Xu H, Huang Q, Wang Y, Hou C, Hou Y, Wang J, Dang F, Zhang J (2020) Tunable cationic vacancies of cobalt oxides for efficient electrocatalysis in Li-O_2 batteries. Adv Energy Mater 10:2001415
5. Yang L, Wu Y, Wu Y, Younas W, Jia J, Cao C (2019) Hierarchical flower-like Fe_2O_3 mesoporous nanosheets with superior electrochemical lithium storage performance. J Energy Storage 23:363–370
6. Hou C, Fan G, Xie X, Zhang X, Sun X, Zhang Y, Wang B, Du W, Fan R (2021) TiN/Al_2O_3 binary ceramics for negative permittivity metacomposites at kHz frequencies. J Alloy Compd 855:157499
7. Xie X, Zhang B, Wang Q, Zhao X, Wu D, Wu H, Sun X, Hou C, Yang X, Yu R, Zhang S, Murugadoss V, Du W (2021) Efficient microwave absorber and supercapacitors derived from puffedrice-based biomass carbon: effects of activating temperature. J Colloid Interf Sci 594:290–303
8. Li Y, Yuan H, Chen Y, Wei X, Sui K, Tan Y (2021) Application and exploration of nanofibrous strategy in electrode design. J Mater Sci Technol 74:189–202
9. Hou C, Hou J, Zhang H, Ma Y, He X, Geng W, Zhang Q (2020) Facile synthesis of $LiMn_{0.75}Fe_{0.25}PO_4$/C nanocomposite cathode materials of lithium-ion batteries through microwave sintering. Eng Sci 11:36–43
10. Idrees M, Liu L, Batool S, Luo H, Liang J, Xu B, Wang S, Kong J (2019) Cobalt-doping enhancing electrochemical performance of silicon/carbon nanocomposite as highly efficient anode materials in lithium-ion batteries. Eng Sci 6:64–76
11. Yan Z, Sun Z, Xia A, Yin R, Huang X, Yue K, Xu H, Zhao G, Qian L (2020) Li_3VO_4/carbon sheets composites from cellulose as an anode material for high performance lithium-ion batteries. Ceram Int 46:2247–2254
12. Yan Z, Sun Z, Yue K, Li A, Qian L (2020) CoO/ZnO nanoclusters immobilized on N-doped 3 D reduced graphene oxide for enhancing lithium storage capacity. J Alloy Compd 836:155443
13. Zhu Y, Zhang S, Sun Y, Xie A, Shen Y (2019) A novel FeC_2O_4-TOP derived porous pillar-like γ-Fe_2O_3/carbon nanocomposite with excellent performance as anode for lithium-ion batteries. Appl Surf Sci 479:1212–1219

14. Pan X, Duan X, Lin X, Zong F, Tong T, Li T, Wang T (2018) Rapid synthesis of Cr-doped γ-Fe_2O_3/reduced graphene oxide nanocomposites as high performance anode materials for lithium ion batteries. J Alloy Compd 732:270–279
15. Wang B, Luan S, Peng Y, Zhou J, Hou L, Gao F (2021) High electrochemical performance of Fe_2O_3@OMC for lithium-ions batteries. Nanotechnology 32:125403
16. Zhang K, Zhu Z, Lin J, Zhang R, Zhao C (2020) One-step simultaneously heteroatom doping and phosphating to construct 3D FeP/C nanocomposite for lithium storage. Appl Surf Sci 500:144055
17. Zhu X, Xu J, Luo Y, Fu Q, Liang G, Luo L, Chen Y, Lin C, Zhao X (2019) $MoNb_{12}O_{33}$ as a new anode material for high-capacity, safe, rapid and durable Li^+ storage: structural characteristics, electrochemical properties and working mechanisms. J Mater Chem A 7:6522–6532
18. Fu Q, Li R, Zhu X, Liang G, Luo L, Chen Y, Lin C, Zhao X (2019) Design, synthesis and lithium-ion storage capability of $Al_{0.5}Nb_{24.5}O_{62}$. J Mater Chem A 7:19862–19871
19. Zhai P, Zhang Y, Wu Y, Gao J, Zhang B, Cao S, Zhang Y, Li Z, Sun L, Hou J (2020) Engineering active sites on hierarchical transition bimetal oxides/sulfides heterostructure array enabling robust overall water splitting. Nat Commun 11:5462
20. Hu M, Lv Q, Lv R (2019) Controllable synthesis of nitrogen-doped graphene oxide by tablet-sintering for efficient lithium/sodium-ion storage. ES Energy Environ 3:45–54
21. Fu Y, Pei X, Yao D, Mo D, Lyu S (2019) Three-dimensional graphene-like carbon prepared from CO_2 as anode material for high-performance lithium-ion batteries. ES Energy Environ 4:66–73
22. Hafez AM, Sheng J, Cao D, Chen Y, Zhu H (2019) Flexible lithium metal anode featuring ultrahigh current density stability with uniform deposition and dissolution. ES Energy Environ 5:85–93
23. Jayanthi S (2019) Studies on ionic liquid incorporated polymer blend electrolytes for energy storage applications. Adv Compos Hybrid Mater 2:351–360
24. Mirabootalebi SO (2020) A new method for preparing buckypaper by pressing a mixture of multi-walled carbon nanotubes and amorphous carbon. Adv Compos Hybrid Mater 3:336–343
25. Naik J, Bhajantri RF, Hebbar V, Rathod SG (2018) Influence of ZrO_2 filler on physico-chemical properties of PVA/$NaClO_4$ polymer composite electrolytes. Adv Compos Hybrid Mater 1:518–529
26. Tian Y, Yang X, Nautiyal A, Zheng Y, Guo Q, Luo J, Zhang X (2019) One-step microwave synthesis of MoS_2/MoO_3 @graphite nanocomposite as an excellent electrode material for supercapacitors. Adv Compos Hybrid Mater 2:151–161
27. Wang Y, Hu Y, Hao X, Peng P, Shi J, Peng F, Sun R (2020) Hydrothermal synthesis and applications of advanced carbonaceous materials from biomass: a review. Adv Compos Hybrid Mater 3:267–284
28. Hou B, Wang Y, Ning Q, Liang H, Yang X, Wang J, Liu M, Zhang J, Wang X, Wu X (2019) Dual-carbon enhanced FeP nanorods vertically grown on carbon nanotubes with pseudocapacitance-boosted electrochemical kinetics for superior lithium storage. Adv Electron Mater 5:1900006
29. Yang F, Gao H, Hao J, Zhang S, Li P, Liu Y, Chen J, Guo Z (2019) Yolk–shell structured FeP@C nanoboxes as advanced anode materials for rechargeable lithium-/potassium-ion batteries. Adv Funct Mater 29:1808291
30. Zhao X, Yang P, Yang L, Cheng Y, Chen H, Liu H, Wang G, Murugadoss V, Angaiah S, Guo Z (2018) Enhanced electrochemical performance of Cu^{2+} doped TiO_2 nanoparticles for lithium-ion battery. ES Mater Manuf 1:67–71
31. Xie P, Liu Y, Feng M, Niu M, Liu C, Wu N, Sui K, Patil RR, Pan D, Guo Z, Fan R (2021) Hierarchically porous Co/C nanocomposites for ultralight high-performance microwave absorption. Adv Compos Hybrid Mater 4:173–185
32. Hou C, Wang B, Murugadoss V, Vupputuri S, Chao Y, Guo Z, Wang C, Du W (2020) Recent advances in Co_3O_4 as anode materials for high-performance lithium-ion batteries. Eng Sci 11:19–30
33. Wu D, Niu Y, Wang C, Wu H, Li Q, Chen Z, Xu B, Li H, Zhang L (2019) γ-Fe_2O_3 nanoparticles stabilized by holey reduced graphene oxide as a composite anode for lithium ion batteries. J Colloid Interf Sci 552:633–639
34. Ju W, Dong C, Jin B, Zhu Y, Wen Z, Jiang Q (2020) Composites of reduced graphene oxide and Fe_2O_3 nanoparticles anchored on MoS_2 nanosheets for lithium storage. ACS Appl Nano Mater 3:9009–9015
35. Xiao X, Zhang Z, Yang K, Mei T, Yan D, Wang X (2021) Design and synthesize hollow spindle Ni-doped Co_9S_8@ZnS composites and their enhanced cycle performance. J Alloy Compd 853:157118
36. Li Y, Li W, Yang C, Tao K, Ma Q, Han L (2020) Engineering coordination polymer-derived one-dimensional porous S-doped Co_3O_4 nanorods with rich oxygen vacancies as high-performance electrode materials for hybrid supercapacitors. Dalton Trans 49:10421–10430
37. Qi X, Yan Z, Liu Y, Li X, He G, Komarneni S (2018) Ni and Co doped yolk-shell type Fe_2O_3 hollow microspheres as anode materials for lithium-ion batteries. Mater Chem Phys 211:452–461
38. Yang J, Zhang Q, Wang Z, Wang Z, Kang L, Qi M, Chen M, Liu W, Gong W, Lu W, Shum PP, Wei L (2020) Rational construction of self-standing sulfur-doped Fe_2O_3 anodes with promoted energy storage capability for wearable aqueous rechargeable NiCo-Fe batteries. Adv Energy Mater 10:2001064
39. Ma C, Fu Z, Deng C, Liao X, He Y, Ma Z, Xiong H (2018) Carbon-coated FeP nanoparticles anchored on carbon nanotube networks as an anode for long-life sodium-ion storage. Chem Commun 54:11348–11351
40. Wang Y, Fu Q, Li C, Li H, Tang H (2018) Nitrogen and phosphorus dual-doped graphene aerogel confined monodisperse iron phosphide nanodots as an ultrafast and long-term cycling anode material for sodium-ion batteries. ACS Sustain Chem Eng 6:15083–15091
41. Han J, Zhu K, Liu P, Si Y, Chai Y, Jiao L (2019) N-doped CoSb@C nanofibers as a self-supporting anode for high-performance K-ion and Na-ion batteries. J Mater Chem A 7:25268–25273
42. Lin J, Zeng C, Lin X, Xu C, Su C (2020) CNT-assembled octahedron carbon-encapsulated Cu_3P/Cu heterostructure by in situ MOF-derived engineering for superior lithium storage: investigations by experimental implementation and first-principles calculation. Adv Sci 7:2000736
43. Wang W, Ma Y, Liu L, Yao S, Wu W, Wang Z, Lv P, Zheng J, Yu K, Wei W, Ostrikov KK (2020) Plasma enabled Fe_2O_3/Fe_3O_4 nano-aggregates anchored on nitrogen-doped graphene as anode for sodium-ion batteries. Nanomaterials 10:782
44. Wu C, Xu Y, Ao L, Jiang K, Shang L, Li Y, Hu Z, Chu J (2020) Robust three-dimensional porous rGO aerogel anchored with ultra-fine α-Fe_2O_3 nanoparticles exhibit dominated pseudocapacitance behavior for superior lithium storage. J Alloy Compd 816:152617
45. Li Y, Fu Y, Chen S, Huang Z, Wang L, Song Y (2019) Porous Fe_2O_3/Fe_3O_4@Carbon octahedron arrayed on three-dimensional graphene foam for lithium ion battery. Compos Part B-Eng 171:130–137
46. Xiu Z, Ma J, Wang X, Gao Z, Meng X (2020) Hierarchical porous Fe_3O_4@N-doped carbon nanoellipsoids with excellent electrochemical performance as anode for lithium-ion batteries. J Solid State Chem 282:121118
47. Hou C, Wang J, Zhang W, Li J, Zhang R, Zhou J, Fan Y, Li D, Dang F, Liu J, Li Y, Liang K, Kong B (2020) Interfacial superassembly of grape-like MnO-Ni@C frameworks for superior lithium storage. ACS Appl Mater Inter 12:13770–13780

48. Hou C, Wang J, Du W, Wang J, Du Y, Liu C, Zhang J, Hou H, Dang F, Zhao L, Guo Z (2019) One-pot synthesized molybdenum dioxide-molybdenum carbide heterostructures coupled with 3D holey carbon nanosheets for highly efficient and ultrastable cycling lithium-ion storage. J Mater Chem A 7:13460–13472
49. Hou C, Tai Z, Zhao L, Zhai Y, Hou Y, Fan Y, Dang F, Wang J, Liu H (2018) High performance MnO@C microcages with a hierarchical structure and tunable carbon shell for efficient and durable lithium storage. J Mater Chem A 6:9723–9736
50. Hou C, Yang W, Xie X, Sun X, Wang J, Naik N, Pan D, Mai X, Guo Z, Dang F, Du W (2021) Agaric-like anodes of porous carbon decorated with MoO_2 nanoparticles for stable ultralong cycling lifespan and high-rate lithium/sodium storage. J Colloid Interf Sci 596:396–407